Continuous Microevolution Accelerates Disease Progression during Sequential Episodes of Infection

Alistair Harrison[1], **Rachael L. Hardison**[1], **Audra R. Fullen**[1], **Rachel M. Wallace**[1], **David M. Gordon**[2], **Peter White**[2], **Ryan N. Jennings**[3], **Sheryl S. Justice**[1,4,*], **Kevin M. Mason**[1,4,5,*]

[1]Center for Microbial Pathogenesis, The Abigail Wexner Research Institute at Nationwide Children's Hospital, Columbus, OH 43205, USA

[2]The Steve and Cindy Rasmussen Institute of Genomic Medicine, The Abigail Wexner Research Institute at Nationwide Children's Hospital, Columbus, OH 43215, USA

[3]College of Veterinary Medicine, The Ohio State University, Columbus, OH 43210, USA

[4]Infectious Disease Institute, The Ohio State University, Columbus, OH 43205, USA

[5]Lead Contact

SUMMARY

Bacteria adapt to dynamic changes in the host during chronic and recurrent infections. Bacterial microevolution is one type of adaptation that imparts a selective advantage. We hypothesize that recurrent episodes of disease promote microevolution through genetic mutations that modulate disease severity. We use a pre-clinical model of otitis media (OM) to determine the potential role for microevolution of nontypeable *Haemophilus influenzae* (NTHI) during sequential episodes of disease. Whole genome sequencing reveals microevolution of hemoglobin binding and lipooligosaccharide (LOS) biosynthesis genes, suggesting that adaptation of these systems is critical for infection. These OM-adapted strains promote increased biofilm formation, inflammation, stromal fibrosis, and an increased propensity to form intracellular bacterial communities (IBCs). Remarkably, IBCs remain for at least one month following clinical resolution of infection, suggesting an intracellular reservoir as a nidus for recurrent OM. Additional approaches for therapeutic design tailored to combat this burdensome disease will arise from these studies.

Graphical Abstract

In Brief

Harrison et al. develop a sequential model of otitis media (OM) to investigate microevolution through genetic mutations that modulate disease severity. OM-adapted strains promote increased biofilm, inflammation, stromal fibrosis, and intracellular bacterial community (IBC) development. IBCs remain one month following clinical resolution of infection, suggesting a nidus for recurrent OM.

INTRODUCTION

Many bacterial pathogens cause chronic, treatment-refractory disease, in part by seeking intracellular refuge from both the host immune system and antibiotic therapies. In addition, bacterial and host elements that dictate the complexity and fitness of these pathogens, the impact on persistence and recurrence, and how chronic sequelae arise from infection are not completely understood. Therefore, the delineation of host-pathogen interactions that promote bacterial microevolution and contribute to bacterial survival during recurrent and chronic infections will inform additional therapeutic approaches.

Nontypeable *Haemophilus influenzae* (NTHI) migration from the nasopharynx to the upper and lower respiratory tract coincides with initiation of diseases such as otitis media (OM), conjunctivitis, sinusitis, and pneumonia, and exacerbates disease severity in patients with chronic obstructive pulmonary disease (COPD) and cystic fibrosis (Duell et al., 2016; Jalalvand and Riesbeck, 2018; Pelton, 2019; Román et al., 2004; Sriram et al., 2018). OM is

the most common bacterial disease of children under 15 years of age, with 700 million cases of acute OM and 300 million cases of chronic suppurative OM each year (Mittal et al., 2015; Tong et al., 2018). In addition, OM is highly recurrent, with children experiencing as many as six episodes of OM by age 7 (Pichichero, 2013), and the potential adaptation that occurs during sequential episodes and the impact on disease progression are unknown. Sequelae that arise from OM include hearing loss and developmental delays in behavior and language, as well as education (Homøe et al., 2019; Schilder et al., 2016). Approximately 65% of all antibiotics prescribed are for the treatment of OM in children less than 2 years old, and 45% in children 2–4 years old (Vaz et al., 2014). As a result, the emergence of antibiotic-resistant strains has led to the prioritization of *Haemophilus influenzae* for the development of additional antibiotics by the World Health Organization (WHO) (Tacconelli et al., 2018). In total, the estimated cost associated with treatment of OM exceeds $4 billion annually in the US (Tong et al., 2018).

Our understanding of the different sequelae of NTHI infection, particularly NTHI persistence, OM chronicity, and recurrence of disease, is limited due to the lack of available model systems. We previously demonstrated that nutritional sequestration influences disease progression and severity, microevolution of NTHI during stationary phase, and establishment of an intracellular NTHI population (Hardison et al., 2018a, 2018b; Szelestey et al., 2013). Host microenvironmental influences on NTHI pathoadaptation and evolution have revealed additional targets for treatment of OM based upon the multiple pathogenic lifestyles revealed in our studies (e.g., biofilm, intracellular) (Hardison et al., 2018a, 2018b; Harrison et al., 2016; Szelestey et al., 2013). In order to evaluate the effect of multiple episodes of OM on the microevolution of NTHI, we established a model system of sequential OM episodes through naive hosts. After four episodes of OM, we observed increased bacterial burden in both the effusion and the associated mucosal tissue. We further observed increased biofilm biomass, suppurative inflammation, and stromal fibrosis. The bacterial genomes collected from the fourth episode were sequenced, compared to the input strain used for the first episode, and mutations were identified and verified in 12 genes. Moreover, in two genes, multiple separate mutations were observed in a single locus. These mutations were categorized into four classes based upon the location and type of mutation: translational phase variation; intragenic single nucleotide polymorphisms (SNPs); insertion; and deletion. Furthermore, the OM-adapted strains display a significant increase in the formation of intracellular bacterial communities (IBCs). Strikingly, IBCs remained for at least 4 weeks following resolution of clinical signs of disease from a single episode of OM. Taken together, our studies demonstrate that NTHI responds to host pressures through microevolution that promotes pathogenic lifestyles. The presence of long-standing IBCs in the middle ear mucosae provides a pre-clinical model to assess mechanisms of recurrence of OM from an intracellular reservoir. In addition, the identification of genes under selection in the host provides additional insight into the disease course and reveals potential targets for therapies.

RESULTS

Sequential Episodes of OM Promote Increased Biofilm Formation and Bacterial Growth during Acute Infection

Our prior studies demonstrated microevolution of NTHI in response to transient limitation of nutrients that promote long-term survival *in vitro* (Hardison et al., 2018a). To determine the types of NTHI-adaptive responses to the myriad of microenvironmental changes during host infection, we established a model of sequential episodes of OM. Following a 7-day infection, NTHI were isolated and sequentially introduced into a second cohort of naive chinchillas. This process was repeated to establish four sequential episodes of OM with two independent lineages (e.g., mucosal and effusion) in biological triplicate (Figure 1A). For each episode of disease, we determined the effect of adaptation on bacterial burden and biofilm formation.

During harvest of the middle ear tissues, we observed an increase in biofilm in the middle ear space with each sequential episode (Figure 1B). The extent of biofilm formation can be gauged by ability to visualize the bony septa present in the inferior bullae (Figure 1C). The biofilm is composed of NTHI and host immune cell infiltrate. For every episode of disease, the increase in biofilm occurred over a 7-day period and was independent of the lineage (effusion or mucosal). In some cases, by the end of episode 4, the biofilm completely filled the inferior space and began to cover the tympanic membrane. The visual changes in biofilm growth was confirmed by quantitative measurement of recovered tissue and associated biofilm, revealing a significant increase in biofilm weight for episode 4 (Figure 1D).

We observed a concurrent increase in the number of bacteria recovered from the middle ear mucosae with each sequential passage with statistical significance observed in episodes 3 and 4 (Figure 1E). Consistent with the increase in mucosae-associated bacteria, we also observed a significant increase in the bacteria recovered from the middle ear effusions in episodes 3 and 4 (Figure 1F). Collectively, these data suggest *in vivo* adaptation of NTHI during sequential episodes of OM (OM-adapted NTHI) promotes both biofilm formation and bacterial burden.

Suppurative Inflammation and Stromal Fibrotic Lesions Are More Severe in Response to Infection with OM-Adapted NTHI

Histopathological assessment of the middle ears revealed woven bone formation during the first episode of OM that remained consistent with each sequential episode (Figure S1). In addition, we observed an increase in goblet cell formation between episodes 1 and 4 that did not reach statistical significance. In marked contrast, host immune cell infiltrate (suppurative inflammation) was observed on day 7 of episode 1 and was significantly increased on day 7 of episode 4 (Figure 2A). As with biofilm formation, the increase in suppurative inflammation was similar between the effusion and mucosal lineages. Independent scoring determined that this difference was statistically significant (Figure 2B). The production of fibrotic lesions in the stroma was also significantly increased during episode 4 as compared with episode 1 (Figures 2C and 2D). These observations suggest that the *in vivo* adaptation

of NTHI due to repeated episodes of infection promotes pathogenesis through modulation of host responses.

Sequential Passage Promotes Microevolution of NTHI

On day 7 of the fourth episode of OM, NTHI were isolated from the mucosae (mucosal lineage, n = 3) or effusions (effusion lineage, n = 3) of the middle ears and subjected to whole genome sequencing. Comparison of whole genome sequences of isolates obtained at the end of episode 4 with the genome of the initial inoculum revealed mutations in a total of 12 genes (Figure 3D). These mutations were validated by Sanger sequencing and categorized into four classes based upon the location and type of mutation: translational phase variation, intragenic SNPs, insertion or deletion (Table S2; Figure 3D). The majority of the mutated genes encode proteins involved in lipooligosaccharide (LOS) production, while three mutated genes encode proteins involved in the import of hemoglobin and hemoglobin-haptoglobin (Figure 3D). The mutations observed indicate that outer membrane surface structures and selective iron transport proteins are under evolutionary pressure during experimental OM (Figure 3D).

Microevolution of Genes Encoding Hemoglobin-Haptoglobin Import during Sequential OM

Of all the iron uptake systems encoded by NTHI, mutations were only identified in genes encoding proteins involved in hemoglobin-haptoglobin binding (Figure 3). These three genes are phase variable with the deletion or insertion of intragenic tetranucleotide repeats. The specific gene modifications and outcomes are presented in Table S2. In the case of *hgpB*, all of the mutations led to the introduction of a premature stop codon that will result in the absence of protein production (Figure 3A). Mutation 2 (loss of a single tetranucleotide repeat) was the predominant variant observed in 4 of 6 lineages. Mutations were observed as early as the end of episode 2 but were observed in four lineages by the end of episode 4. For *hgpC*, we observed a loss of one repeat in all isolates except ML3, where five repeats were lost (Figure 3B). Interestingly, in all cases, these mutations resulted in the production of protein (phase variation from OFF to ON) during the first episode. In ML3, the gene lost an additional four tetranucleotide repeats during episode 4 that results in a premature stop codon and a predicted loss of protein function (Figure 3B). For *hgpD*, the gene remained OFF in the majority of isolates with the same number of repeats asthe input strain (Figure 3C). However, in one case, EL2, a single repeat was inserted that results in protein production.

The continuous production of HgpC suggests an initial benefit in protein function during early OM. Despite the phase variation in regulation of *hgpC*, the gene remained in frame throughout the study (Figure 3B). Inaddition, thisgeneappears tobe under continuous selective pressure, as seven SNPs are acquired (Figure 4A; Table S2). Mutations were observed as early as the first episode, but by the end of episode 4 all samples contain at least one additional mutation and as many as three mutations (Figure 4B). Interestingly, all of the SNPs mapped to the extracellular loops of the 3-dimensional predicted structure of HgpC (Figure 4C). These mutations did not alter the integral membrane pore, suggesting that these mutations affect the affinity for hemoglobin or hemoglobin-haptoglobin binding and likely

the rate of transport. Taken together, it appears that HgpC is the preferred hemoglobin-haptoglobin binding protein during recurrent episodes of acute OM.

The Microevolution of Glycosyltransferase Encoding Genes during Sequential OM

The LOS biosynthetic pathway appears to be under selective pressure during sequential episodes of OM. The structure of LOS was predicted from prior studies using wild-type and derivative strains of *H. influenzae* Rd (Figure 5A) (Wong and Akerley, 2012). We observed mutations in all of the predicted sugar modification enzymes that extend from the third heptose of the inner core of LOS (Figure 5A). Of these genes, *lgtC*, *lic2A*, and *lic3A2* are phase variable (Figure 5B). Mutations in *lic2A* and *lic3A2* that switch the gene OFF are acquired as early as during the first episode. By the end of episode 4, in conjunction with *lgtC*, there are phase-variable mutations in all lineages that truncate sugar modification of the lipid A and inner core of LOS.

In addition to the phase variation observed in the genes associated with LOS, SNPs and short insertions were observed in the non-phase–variable LOS-associated genes. Unlike all the other mutations presented, we did not observe congruence between the whole genome sequencing and Sanger sequencing for *lpA* alleles 1 and 2. The mutations result in a string of thymidine nucleotides that are more difficult to resolve with bioinformatics approaches (Baptista and Kissinger, 2019). The *lpsA* gene acquired two independent SNPs, or two small insertions (Figure 6B; Table S2) in five of six lineages by episode 4. The one lineage that did not predominantly convert to any of the mutant forms of *lpsA* (EL2) acquired a mutation in *lic2A* (Figures 5C and 6A), which would result in an LOS structure truncated at the first glucose. Interestingly, three of four *lpsA* mutations resulted in a frameshift or introduction of an amber stop codon, suggesting that the protein is not functional. The fourth mutation resulted in the change of the alanine at position 178 to a valine (Table S2). A mutation in *lgtD* was also observed in EL2 during the third episode, the lineage that did not predominantly convert to a mutant form of *lspA* (Figures 6A and 6B). In addition, mutations 1, 2, and 4 within *lpsA* were detected in at least four lineages, suggesting that these mutations have some benefit during infection. Collectively, these mutations result in a truncation of the LOS in all six lineages.

The Gene Encoding an Autotransporter Exhibits Microevolution during Sequential OM

The understudied *lav* gene is phase variable and with sequence similarity to invasion genes in *Neisseria* (Zhang et al., 2017). In 50% of the lineages, *lav* lost a single tetranucleotide repeat in the first episode of OM, introducing a premature stop codon (Figure S2A, upper panel). In one lineage, ML2, there is a second mutation that resulted in a gain of three repeats during episode 1 but did not affect the reading frame (Table S2). However, *lav* transitions to the OFF variation in ML2 by the end of episode 4 (Figure S2A, lower panel). In the ML3 lineage, there were no detectible mutations within *lav*, even at the end of episode 4. Taken together, by the end of episode 4, in four of the six lineages the *lav* gene was observed in the OFF variation. Interestingly, the two lineages that maintain Lav function were isolated from the same ear at the end of episode 1. The pressure to maintain *lav* in the OFF orientation suggests that there is some benefit during recurrent episodes of OM when Lav is not produced.

The Microevolution of Genes of Unknown Function during Sequential OM

We observed mutations in three putative genes of unknown function (Table S2; Figure S2). NTHI0512 encodes a putative acyltransferase with only acquired mutations in lineages EL2 and ML1 (Figure S2B). NTHI1750, which encodes for a putative glycosyl transferase, maintained the parental genotype in five of six lineages of the samples by the end of episode 4 (Figure S2C). Finally, in the putative apolipophorin, NTHI1667, deletions were detected in all episodes of the EL3 and ML3 lineages (Figure 6D). Interestingly, these are the lineages that retained Lav function; the correlation of these specific systems remains unclear.

Intracellular Reservoirs of NTHI Were Observed Weeks following Clinical Resolution of Experimental OM

We observed IBCs within middle ear epithelial cells following transient restriction for heme-iron (Hardison et al., 2018a; Szelestey et al., 2013). Intracellular bacteria have been observed within clinical biopsies obtained from middle ear epithelium of children with chronic or recurrent OM (Thornton et al., 2011). Therefore, we sought to determine whether adaptation during sequential episodes of OM promotes IBC formation. Consistent with our prior observations, we observed IBCs within the middle ear epithelium during the first episode of OM (Figures 7A and 7B). We observed a significant increase in the number of IBCs on day 7 of the fourth episode from ears infected with either effusion or mucosal lineage (Figure 7B), suggesting that the adaptation during prior episodes of OM promotes formation of IBCs.

We previously demonstrated that IBCs of NTHI significantly increase over time during the natural course of acute OM (Hardison et al., 2018a). To determine the longevity of IBCs, we evaluated the presence of IBCs during the natural course of OM on day 49 (week 7) using the parental strain 86–028NP. The absence of effusion is a clinical indicator of disease resolution. In this model, resolution of OM typically occurs prior to day 28 (Figure 7C, gray shaded area). IBCs were readily detected on day 49, 3 weeks following clinical resolution of OM (Figure 7C). Consistent with clinical resolution, decreased inflammation coincided with restoration of mucosal integrity and the absence of a biofilm (Figure 7C, insets). Thus, we observed the presence of IBCs for at least one month following apparent disease resolution, suggesting a potential nidus for recurrent OM.

DISCUSSION

Prior to these studies, pre-clinical models that provide insight into the mechanisms of NTHI persistence, OM chronicity, and recurrence of disease were limited. This model of sequential episodes of OM using naive hosts for each subsequent infection advances our understanding of OM pathogenesis through the observation of increased disease severity and establishment of an intracellular NTHI reservoir. In this model system, we observed that host microenvironmental cues promote NTHI pathoadaptation through microevolution. Interestingly, the phenotypes observed are associated with mutations that affect the function of surface-exposed moieties, suggesting a role for these molecules at the host pathogen interface that modulates responses and disease severity. In addition, our observations indicate that host-derived pressures can modulate the formation of intracellular bacterial

reservoirs, providing additional insight into the role of bacterial adaptation on intracellular lifestyles.

NTHI are heme-auxotrophs reliant on the import of heme, heme-containing moieties, or the components of heme for survival (Stojiljkovic and Perkins-Balding, 2002). NTHI strain 86–028NP encodes 19 proteins predicted to participate in heme and iron utilization (Harrison et al., 2005). Of these, we observed microevolution of three hemoglobin binding proteins (HgpB, HgpC, and HgpD). Despite the essential requirement for heme acquisition from molecules like hemoglobin, few studies have investigated which systems are utilized during infection. Prior studies using complete gene knockouts of all three hemoglobin-haptoglobin encoding genes resulted in decreased utilization of hemoglobin and hemoglobin-haptoglobin for a type B strain of *Haemophilus* under laboratory growth conditions (Morton et al., 1999). Furthermore, inactivation of all three hemoglobin/haptoglobin binding proteins had minimal effect on the pathogenesis of NTHI during septicemia. While prior studies evaluated complete gene knockouts, our system allowed for microevolutionary adaptation of genes that provides additional insight into the mechanisms used for hemoglobin utilization during OM. The natural course of the sequential OM episodes demonstrated selective pressures (e.g., fluctuations in hemoglobin-haptoglobin availability) for phase variation, and the acquisition of SNPs that allow for additional modulation of hemoglobin/haptoglobin binding activity. Our results provide evidence for the importance of HgpB and HgpC in hemoglobin-haptoglobin utilization during OM. Our studies indicate that HgpD is not produced in any of the lineages evaluated, suggesting that HgpD does not contribute to hemoglobin-haptoglobin uptake during OM. In contrast, we observed a shift from production of HgpB to HgpC during early episodes of OM, suggesting that the altered microenvironment leads to a preferential acquisition of hemoglobin-haptoglobin through the HgpC protein in recurrent episodes of OM, suggesting adaptation to the changes in hemoglobin and hemoglobin-haptoglobin availability during infection. This suggestion is further supported by the observation that HgpC continues to acquire amino acids substitutions in subsequent rounds of OM. Interestingly, all of the substitutions in HgpC map to the external surface of the predicted barrel structure. It is intriguing to speculate that these mutations modulate the affinity and transport of hemoglobin and hemoglobin-haptoglobin. We speculate that the presence of inflammation may provide an increased nutritional pool in a restricted environment. We observe that two hemoglobin acquisition proteins are OFF and one that remains ON. The continuous accumulation of mutations in *hgpC* suggests that the regulation of import is not directly based upon the availability of iron-containing molecules, but is controlled to promote survival during infection yet prevent toxicity. Ongoing studies will determine the contribution of each mutation toward HgpC function as well as the independent contribution of HgpC during pathogenesis.

LOS is an important modulator of the host immune responses and provides protection from host innate immune effectors (Gaultier et al., 2017; Tong et al., 2001). Previous studies suggest that truncation of the LOS outer core prevents binding by IgM and reduces serum sensitivity (Jackson et al., 2019). Thus, we speculate that the mutations identified are under selective pressure of these and potentially other (e.g., antimicrobial peptides) host immune mediators. Genetic comparisons of the seven phase-variable genes associated with LOS from invasive NTHI clinical isolates revealed that *lic2A* was primarily phase OFF (Phillips

et al., 2019). Our data suggest that during sequential episodes of OM, half the genes under selective pressure were involved in the biosynthesis of the outer core of the carbohydrate moiety. In all lineages, we observed mutations that would result in a partial or complete truncation of the LOS after the third heptose (Figure 5). In other bacterial species, truncation of LOS results in higher elicitation of cytokines from epithelial cells (Han et al., 2013). This suggests that the increased host responses observed in the later episodes of OM may be due, at least in part, to the truncation of LOS in the OM-adapted strains. The causal effect of LOS truncation on the magnitude of the innate immune response is unclear and currently under investigation.

We also observed evolution of the understudied autotransporter Lav. The cargo domain of the NTHI Lav is predicted to remain membrane tethered and has a helix-turn-helix motif, suggesting a potential role for binding to extracellular DNA. A closely related ortholog in *Neisseria meningitidis* promotes biofilm formation and reduces transmigration through epithelial cells (Arenas et al., 2016). The observation that a Lav ortholog reduces invasion is consistent with our observation of increased IBC formation in the OM-adapted strains that are primarily in the OFF status. The potential ligand of Lav and a causal role in IBC formation is currently under investigation.

Interestingly, hemoglobin uptake and LOS biosynthesis exhibit microevolution in human infection studies. Comparison of isogenic strains of NTHI obtained from the nasopharynx and from bronchoalveolar lavage fluid of children suffering bronchiectasis or chronic suppurative lung disease revealed a loss of function of *hgpB* due to a frameshift in the phase-variable region, and a loss of *lic3A* function involved in LOS biosynthesis (Aziz et al., 2019). Similarly, comparison of sequential isolates obtained from the lungs of subjects with COPD revealed phase variation that resulted in the loss of *lex1* (*lic2A*), in half of the paired isolates (Pettigrew et al., 2018). As with our study, these sequential isolates also demonstrate that *hgpB* is not functional. In our study, we were able to determine that the transition from ON to OFF for *hgpB* occurs during the later episodes of OM, suggesting that this is an adaptive response to the changing environment. In contrast to the continual microevolution of *hgpC* during OM presented here, *hgpC* was primarily out of frame from isogenic isolates obtained from COPD, suggesting that this is not the preferred uptake mechanism in the lung. In the case of COPD isolates, *hgpA* (ortholog of *hgpD*) appears to undergo continuous mutation in two of the pairs, leading to protein truncation. Taken together, NTHI appears to prefer different proteins for the utilization of hemoglobin-haptoglobin in the middle ear and the lung. The similarity in hotspots of microevolution between human and pre-clinical systems indicates that mechanistic studies in the pre-clinical model will translate to the human infection.

Our understanding of the different sequelae of NTHI infection, particularly NTHI persistence, OM chronicity, and recurrence of disease, is limited due to the lack of available model systems. Moreover, the molecular mechanisms that underlie hearing loss as a consequence of infection are poorly understood. There is an association of stromal fibrosis with the benign growth in the middle ear epithelium, cholesteatoma formation (Lang et al., 1997). We speculate that the bulk of fibrotic tissue accumulation in the middle ear impacts

hearing. The model presented here can be used to delineate the contributions of fibrosis and suppurative inflammation in hearing loss.

Clinically, resolution of OM coincides with the clearance of middle ear fluid, which presumes absence of viable bacteria. In contrast to this clinical paradigm, we observed the presence of IBCs a month after resolution of clinical disease, suggesting the presence of a mucosal reservoir as a potential nidus for recurrence. A deeper understanding of microevolution of NTHI during disease will give insight into how IBCs develop and how the bacteria survive for protracted periods of time within the host. In addition, use of these adapted isolates to inoculate naive hosts revealed that these mutations redirect the outcome of the infection with increased biofilm formation, suppurative inflammation, fibrosis, and IBC formation. These studies provide a platform to elucidate the causal effect of strain adaption during sequential episodes of OM. Given that OM is a highly recurrent disease, these observations can provide insight into how subsequent episodes can cause more severe disease even by strains that are considered identical. This is of particular interest, given our observation of a reservoir of OM-adapted strains in the form of IBCs that could serve as the nidus for recurrent infections, providing a paradigm for the recurrence of OM. Further characterization of how NTHI strains enter this chronic lifestyle will ultimately reveal targets for therapeutic modalities in the treatment of this burdensome disease.

STAR★METHODS

LEAD CONTACT AND MATERIALS AVAILABILITY

Further information and requests for resources and reagents should be directed to and will be fulfilled by the Lead Contact, Kevin M. Mason (Kevin.Mason@nationwidechildrens.org). All unique/stable reagents generated in this study are available from the Lead Contact with a completed Materials Transfer Agreement. Commercially available reagents are indicated in the Key Resources Table.

EXPERIMENTAL MODEL AND SUBJECT DETAILS

Strains and media—For routine culturing, strains were grown on chocolate agar (Thermo Fisher Scientific, Waltham, MA). All growth was performed at 37°C in 5% CO_2. For routine liquid culture, NTHI was grown in BHI supplemented with 2 μg/mL of NAD and 2 μg/mL of heme (sBHI). NTHI strain 86–028NP is a minimally passaged, fully sequenced, clinical isolate that has been extensively characterized in the chinchilla model of human otitis media (Harrison et al., 2005; Mason et al., 2006; Sirakova et al., 1994). During the course of the study, the input strain of 86–029NP was subjected to whole genome sequencing for comparison with the adapted strains. The 86–028NP input strain displayed the expected sequence from prior studies.

Ethics Statement—Animal experiments were completed in adherence to the accredited conditions in the Guide for the Care and Use of Laboratory Animals of the National Institutes of Health. The protocol was approved by the Institutional Animal Care and Use Committee at the Research Institute at Nationwide Children's Hospital (Welfare Assurance Number A3544–01), AR13–00026. All experimental procedures were performed under

anesthesia (xylazine and ketamine administration) and all efforts made to minimize suffering.

Chinchilla lanigera—Adult outbred chinchillas of equally distributed mixed sex were purchased from the Rauscher ranch (LaRue, OH) as approved by the IACUC. The precise age range is not indicated as the rancher does not record ages of the individual animals. The mean weight of the animals used in this study was 703 ± 30 g. The chinchillas are housed individually in filter top cages, with corncob bedding in a biosafety level 2 facility. Animals are provided *ad libidum* access to approved chinchilla chow and water. Chinchillas are provided with enchrichment (e.g., toys), straw and approved treats. Individuals were randomly assigned to each cohort, with attention to similarity in sex distribution between cohorts. The *chinchilla lanigera* genome is publicly available (Shimoyama et al., 2016).

METHOD DETAILS

Preclinical model of sequential episodes of otitis media—NTHI strain 86–028NP was grown on chocolate agar overnight at 37°C, 5% CO_2. NTHI was resuspended in 0.9% (w/v) sodium chloride in non-pyrogenic sterile water (Pfizer, New York, NY) to an optical density of 0.65 measured at 490 nm and diluted for inoculation. Three chinchillas each were inoculated with 86–028NP. Approximately 1000 colony forming units (CFUs) of 86–028NP in 300 μl volumes were transbullarly inoculated into each ear under intramuscular administration of a ketamine/xylazine anethesia (dose) in the morning. Animals were placed on a warming blanket until signs of alertness were observed (e.g., voluntary movement) and replaced into the home cage. On the morning of day 7 post-inoculation, middle ear effusions were collected from the inferior bullae by epitympanic tap. Following dissection, the left ear was placed in 4% paraformaldehyde in Dulbecco's phosphate buffered saline (DPBS; Corning, Manassas, VA). The mucosa of the right middle ears were removed, weighed, and tissues were disrupted using M1 homogenizer tubes. Middle ear effusions and mucosal homogenates were serially diluted in 0.9% sterile saline, plated on chocolate agar to enumerate viable bacterial burden. The bacterial burden of tissue homogenates was normalized for weight of the recovered tissue. Bacteria recovered from the effusions are reported as CFU/ml. After assessing bacterial burden, approximately 300 NTHI colonies were recovered from the plate, resuspended in 0.9% sterile saline and diluted to an optical density of 0.65 measured at 490 nm. The suspensions were then further diluted to provide an inoculum of approximately 5000 CFU in 300 μl of saline. The inoculum of the sequential episodes of OM was increased to ensure that minor population of adapted NTHI would be included in the inoculum. The remaining culture was frozen at −80°C. The experimental design included two parallel lineages to evaluate potential differences in the microenvironment of the effusion and the mucosal-associated biofilms. The inoculum for each of the middle ears in the effusion lineage were obtained from bacteria recovered only from the effusion of the ear at the time of sacrifice. The inoculum for each of the middle ears in the mucosal lineage were obtained from bacteria recovered only from the mucosal homogenates at the time of harvest. All experiments were performed in biological triplicate.

Longevity of intracellular bacterial communities in the middle ear—Chinchillas were infected as described above and monitored for clinical signs of otitis media via video

otoscopy (i.e., middle ear inflammation, tympanic membrane pathology, presence of effusion) on days 7, 14, 21 and 28 post-infection. Middle ears were harvested on Day 49 post-infection and prepared for visualization of intracellular bacterial communities in middle ear mucosa as described below.

Histopathology—Processing of middle ears for histopathological assessment for markers of OM disease severity was carried out as described in Harrison et al. (2016). Briefly, fixed middle ear bullae were decalcified in 0.35 M Tris/EDTA solution and embedded in paraffin. Thin sections were deparaffinized in xylene and stained with hematoxylin and eosin, periodic-acid Schiff, or trichrome. Slides were mounted and visualized on an Axio Lab.A1 light microscope using an Axiocam ERc 5 s camera (Carl Zeiss Inc., Thornwood, NY). Histopathology was scored by a clinical veterinary pathologist that was provided coded slides and was blinded to the design of the study.

Visualization of intracellular bacterial communities in middle ear mucosal tissue—Quantification of IBCs was carried out as detailed in Hardison et al. (2018b). Thin sections from fixed middle ears were deparaffinized in xylene and antigen-retrieval was performed as described in Harrison et al. (2016) followed by treatment with 0.01% sodium boro-hydride (Thermo Fisher Scientific) in DPBS for 10 minutes to inhibit inherent fluorescence due to aldehyde production. Slides were then incubated for 10 minutes in CAS Block (Thermo Fisher Scientific) to prevent non-specific staining followed by a 30-minute incubation with Image-iT FX Signal Enhancer (Thermo Fisher Scientific). NTHI were visualized with a chinchilla primary antibody raised against total outer membrane proteins [OMP; (Raffel et al., 2013)] combined with Protein A conjugated with Alexa Fluor 488 (Life Technologies, Grand Island, NY), and host cell membranes were visualized using wheat germ agglutinin (WGA) conjugated with Alexa Fluor 594 (Life Technologies, Grand Island, NY) and DNA was counterstained with Hoescht 33342 (Life Technologies). Photobleaching was reduced by the addition of ProLong Gold antifade (Thermo Fisher Scientific) prior to addition of the coverslip and tissues were imaged with an Axiovert 200M inverted epifluoresence microscope equipped with the Apotome attachment for improved fluorescence resolution (Carl Zeiss, Inc.). Controls for specificity of the antibody were performed as described in Hardison et al. (2018b). For each ear, IBCs were manually counted in each of three thin sections by two investigators.

Whole genome sequencing—Whole genome sequencing was performed on pooled bacteria isolated from middle ear effusion or mucosal homogenates as previously described (Hardison et al., 2018a). Genomic DNA was purified using a Gentra Puregene Yeast/Bact. Kit (QIAGEN, German-town, MD). Sequencing libraries were prepared and sequenced using paired end 300bp chemistry on the MiSeq platform (Illumina, San Diego, CA). Nucleotide variants were identified using the Churchill algorithm (Kelly et al., 2015) and the percentage of reads that differ from the reference genome was calculated. The number of reads and genomic coverage for each of the 6 lineages are as follows: EL1, 5,790,619 reads, 908 × coverage; EL2, 5,598,782 reads, 878 × coverage; EL3, 4,514,586 reads, 708 × coverage; ML1, 5,360,632 reads, 840 × coverage; ML2, 3,855,530 reads, 604 × coverage; ML3, 4,162,237 reads, 652 × coverage.

Sanger sequencing—Nucleotide variants were validated by three independent technical replicates of Sanger sequencing (Erofins, Louiville, KY). Primers used in the Sanger sequencing are detailed in Table S1.

QUANTIFICATION AND STATISTICAL ANALYSIS

Statistical significance was determined using a two-tailed Student's t test with the mean and standard error of the mean (linear scale) or geometric mean (logarithmic scale) indicated (GraphPad Prism, La Jolla, CA).

DATA AND CODE AVAILABILITY

The accession number for the whole genome sequence data of the adapted strains has been uploaded to the National Center for Biotechnology Information (NCBI) Sequence Read Archive (SRA) (SRA: PRJNA576916).

Supplementary Material

Refer to Web version on PubMed Central for supplementary material.

ACKNOWLEDGMENTS

REFERENCES

Arenas J, Paganelli FL, Rodríguez-Castaño P, Cano-Crespo S, van der Ende A, van Putten JP, and Tommassen J (2016). Expression of the gene for autotransporter autb of *Neisseria meningitidis* affects biofilm formation and epithelial transmigration. Front. Cell. Infect. Microbiol 6, 162. [PubMed: 27921012]

Aziz A, Sarovich DS, Nosworthy E, Beissbarth J, Chang AB, Smith-Vaughan H, Price EP, and Harris TM (2019). Molecular signatures of non-typeable *Haemophilus influenzae* lung adaptation in pediatric chronic lung disease. Front. Microbiol 10, 1622. [PubMed: 31379777]

Baptista RP, and Kissinger JC (2019). Is reliance on an inaccurate genome sequence sabotaging your experiments? PLoS Pathog. 15, e1007901. [PubMed: 31513692]

Duell BL, Su YC, and Riesbeck K (2016). Host-pathogen interactions of nontypeable *Haemophilus influenzae*: from commensal to pathogen. FEBS Lett. 590, 3840–3853. [PubMed: 27508518]

Gaultier GN, Colledanchise KN, Alhazmi A, and Ulanova M (2017). The immunostimulatory capacity of nontypeable *Haemophilus influenzae* lipooligosaccharide. Pathog. Immun 2, 34–49. [PubMed: 30993246]

Han Y, Li Y, Chen J, Tan Y, Guan F, and Wang X (2013). Construction of monophosphoryl lipid A producing *Escherichia coli* mutants and comparison of immuno-stimulatory activities of their lipopolysaccharides. Mar. Drugs 11, 363–376. [PubMed: 23434832]

Hardison RL, Harrison A, Wallace RM, Heimlich DR, O'Bryan ME, Sebra RP, Pinkett HW, Justice SS, and Mason KM (2018a). Microevolution in response to transient heme-iron restriction enhances intracellular bacterial community development and persistence. PLoS Pathog. 14, e1007355. [PubMed: 30332468]

Hardison RL, Heimlich DR, Harrison A, Beatty WL, Rains S, Moseley MA, Thompson JW, Justice SS, and Mason KM (2018b). Transient nutrient deprivation promotes macropinocytosis-dependent intracellular bacterial community development. MSphere 3, e00286–18. [PubMed: 30209128]

Harrison A, Dubois LG, St John-Williams L, Moseley MA, Hardison RL, Heimlich DR, Stoddard A, Kerschner JE, Justice SS, Thompson JW, and Mason KM (2016). Comprehensive proteomic and metabolomic signatures of nontypeable *Haemophilus influenzae*-induced acute otitis media reveal bacterial aerobic respiration in an immunosuppressed environment. Mol. Cell. Proteomics 15, 1117–1138. [PubMed: 26711468]

Harrison A, Dyer DW, Gillaspy A, Ray WC, Mungur R, Carson MB, Zhong H, Gipson J, Gipson M, Johnson LS, et al. (2005). Genomic sequence of an otitis media isolate of nontypeable *Haemophilus influenzæ*: comparative study with *H. influenzae* serotype D, strain KW20. J. Bacteriol 187, 4627–4636. [PubMed: 15968074]

Homøe P, Heidemann CH, Damoiseaux RA, Lailach S, Lieu JEC, Phillips JS, and Venekamp RP (2019). Panel 5: Impact of otitis media on quality of life and development. Int. J. Pediatr. Otorhinolaryngol, Published online December 20, 2019.

Jackson MD, Wong SM, and Akerley BJ (2019). Underlying glycans determine the ability of sialylated lipooligosaccharide to protect nontypeable *Haemophilus influenzae* from serum IgM and complement. Infect. Immun 87, e00456–19. [PubMed: 31405955]

Jalalvand F, and Riesbeck K (2018). Update on non-typeable *Haemophilus influenzae*-mediated disease and vaccine development. Expert Rev. Vaccines 17, 503–512. [PubMed: 29863956]

Kelley LA, Mezulis S, Yates CM, Wass MN, and Sternberg MJ (2015). The Phyre2 web portal for protein modeling, prediction and analysis. Nat. Protoc 10, 845–858. [PubMed: 25950237]

Kelly BJ, Fitch JR, Hu Y, Corsmeier DJ, Zhong H, Wetzel AN, Nord-quist RD, Newsom DL, and White P (2015). Churchill: an ultra-fast, deterministic, highly scalable and balanced parallelization strategy for the discovery of human genetic variation in clinical and population-scale genomics. Genome Biol. 16, 6. [PubMed: 25600152]

Lang S, Schilling V, Wollenberg B, Mack B, and Nerlich A (1997). Localization of transforming growth factor-beta-expressing cells and comparison with major extracellular components in aural cholesteatoma. Ann. Otol. Rhinol. Laryngol 106, 669–673. [PubMed: 9270431]

Mason KM, Bruggeman ME, Munson RS, and Bakaletz LO (2006). The non-typeable *Haemophilus influenzae* Sap transporter provides a mechanism of antimicrobial peptide resistance and SapD-dependent potassium acquisition. Mol. Microbiol 62, 1357–1372. [PubMed: 17064364]

Mittal R, Lisi CV, Gerring R, Mittal J, Mathee K, Narasimhan G, Azad RK, Yao Q, Grati M, Yan D, et al. (2015). Current concepts in the pathogenesis and treatment of chronic suppurative otitis media. J. Med. Microbiol 64, 1103–1116. [PubMed: 26248613]

Morton DJ, Whitby PW, Jin H, Ren Z, and Stull TL (1999). Effect of multiple mutations in the hemoglobin- and hemoglobin-haptoglobin-binding proteins, HgpA, HgpB, and HgpC, of *Haemophilus influenzae* type b. Infect. Immun 67, 2729–2739. [PubMed: 10338475]

Pelton S (2019). Acute Otitis Media in Children: Epidemiology, Microbiology, Clinical Manifestations, and Complications, Torchia MM, ed. (UpToDate Inc). https://www.uptodate.com/index.

Pettigrew MM, Ahearn CP, Gent JF, Kong Y, Gallo MC, Munro JB, D'Mello A, Sethi S, Tettelin H, and Murphy TF (2018). *Haemophilus influenzae* genome evolution during persistence in the human airways in chronic obstructive pulmonary disease. Proc. Natl. Acad. Sci. USA 115, E3256–E3265. [PubMed: 29555745]

Phillips ZN, Brizuela C, Jennison AV, Staples M, Grimwood K, Seib KL, Jennings MP, and Atack JM (2019). Analysis of invasive nontypeable *Haemophilus influenzae* isolates reveals selection for the expression state of particular phase-variable lipooligosaccharide biosynthetic genes. Infect. Immun 87, e00093–19. [PubMed: 30833337]

Pichichero ME (2013). Otitis media. Pediatr. Clin. North Am 60, 391–407. [PubMed: 23481107]

Raffel FK, Szelestey BR, Beatty WL, and Mason KM (2013). The *Haemophilus influenzae* Sap transporter mediates bacterium-epithelial cell homeostasis. Infect. Immun 81, 43–54. [PubMed: 23071138]

Román F, Cantón R, Pérez-Vázquez M, Baquero F, and Campos J (2004). Dynamics of long-term colonization of respiratory tract by *Haemophilus influenzae* in cystic fibrosis patients shows a marked increase in hypermutable strains. J. Clin. Microbiol 42, 1450–1459. [PubMed: 15070988]

Schilder AG, Chonmaitree T, Cripps AW, Rosenfeld RM, Casselbrant ML, Haggard MP, and Venekamp RP (2016). Otitis media. Nat. Rev. Dis. Primers 2, 16063. [PubMed: 27604644]

Shimoyama M, Smith JR, De Pons J, Tutaj M, Khampang P, Hong W, Erbe CB, Ehrlich GD, Bakaletz LO, and Kerschner JE (2016). The Chinchilla Research Resource Database: resource for an otolaryngology disease model. Database (Oxford) 2016, baw073. [PubMed: 27173523]

Sirakova T, Kolattukudy PE, Murwin D, Billy J, Leake E, Lim D, DeMaria T, and Bakaletz L (1994). Role of fimbriae expressed by nontypeable *Haemophilus influenzae* in pathogenesis of and protection against otitis media and relatedness of the fimbrin subunit to outer membrane protein A. Infect. Immun 62, 2002–2020. [PubMed: 7909539]

Sriram KB, Cox AJ, Sivakumaran P, Singh M, Watts AM, West NP, and Cripps AW (2018). Non-typeable *Haemophilus influenzae* detection in the lower airways of patients with lung cancer and chronic obstructive pulmonary disease. Multidiscip. Respir. Med 13, 11. [PubMed: 29657714]

Stojiljkovic I, and Perkins-Balding D (2002). Processing of heme and heme-containing proteins by bacteria. DNA Cell Biol. 21, 281–295. [PubMed: 12042068]

Szelestey BR, Heimlich DR, Raffel FK, Justice SS, and Mason KM (2013). Haemophilus responses to nutritional immunity: epigenetic and morphological contribution to biofilm architecture, invasion, persistence and disease severity. PLoS Pathog. 9, e1003709. [PubMed: 24130500]

Tacconelli E, Carrara E, Savoldi A, Harbarth S, Mendelson M, Monnet DL, Pulcini C, Kahlmeter G, Kluytmans J, Carmeli Y, et al.; WHO Pathogens Priority List Working Group (2018). Discovery, research, and development of new antibiotics: the WHO priority list of antibiotic-resistant bacteria and tuberculosis. Lancet Infect. Dis 18, 318–327. [PubMed: 29276051]

Thornton RB, Rigby PJ, Wiertsema SP, Filion P, Langlands J, Coates HL, Vijayasekaran S, Keil AD, and Richmond PC (2011). Multi-species bacterial biofilm and intracellular infection in otitis media. BMC Pediatr. 11, 94. [PubMed: 22018357]

Tong HH, Chen Y, James M, Van Deusen J, Welling DB, and DeMaria TF (2001). Expression of cytokine and chemokine genes by human middle ear epithelial cells induced by formalin-killed *Haemophilus influenzae* or its lipooligosaccharide *htrB* and *rfaD* mutants. Infect. Immun 69, 3678–3684. [PubMed: 11349030]

Tong S, Amand C, Kieffer A, and Kyaw MH (2018). Trends in healthcare utilization and costs associated with acute otitis media in the United States during 2008–2014. BMC Health Serv. Res 18, 318. [PubMed: 29720156]

Vaz LE, Kleinman KP, Raebel MA, Nordin JD, Lakoma MD, Dutta-Linn MM, and Finkelstein JA (2014). Recent trends in outpatient antibiotic use in children. Pediatrics 133, 375–385. [PubMed: 24488744]

Wong SM, and Akerley BJ (2012). Genome-scale approaches to identify genes essential for *Haemophilus influenzae* pathogenesis. Front. Cell. Infect. Microbiol 2, 23. [PubMed: 22919615]

Zhang A, Zhao P, Zhu B, Shi F, Xu L, Gao Y, Xie N, and Shao Z (2017). Characterization and Distribution of the *autB* Gene in *Neisseria meningitidis.* Front. Cell. Infect. Microbiol 7, 436. [PubMed: 29057217]

Author Manuscript

Author Manuscript

Author Manuscript

Author Manuscript

Highlights

- Establishment of a model for sequential episodes of otitis media

- *In vivo*-adapted *Haemophilus* promotes biofilm formation, inflammation, and fibrosis

- Microevolution of hemoglobin uptake and lipooligosaccharide biosynthesis genes

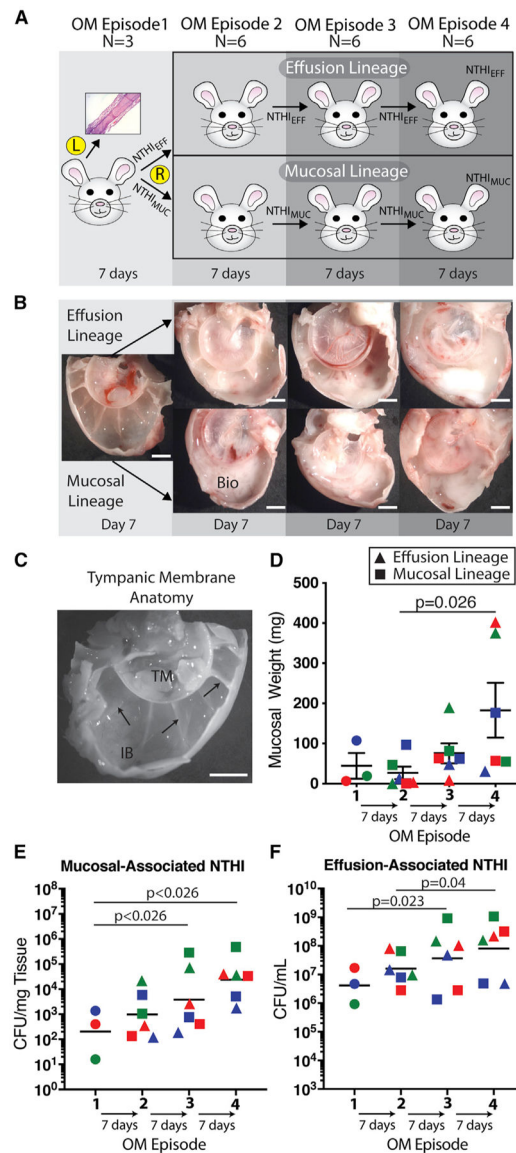- Intracellular bacterial communities remain following clinical resolution of disease

Figure 1. *In Vivo* Adaptation of NTHI

(A) NTHI was sequentially passaged through four episodes of OM. NTHI was recovered from either the effusion ($NTHI_{EFF}$) or the mucosal ($NTHI_{MUC}$) homogenates to generate two parallel lineages, with three biological replicates (n = 6). The left ear (L) was processed for histological examination (see inset) and the NTHI was recovered from the right ear (R). Each episode was allowed to progress for 7 days.

(B) Representative images of the exposed middle ear lumen from each of the OM episodes. Images were obtained on day 7 prior to any tissue harvest from both the effusion and mucosal lineages. Biofilm (Bio).

(C) Diagrammatic representation of the anatomy of the chinchilla middle ear. Tympanic membrane (TM), inferior bullae (IB), and bony septa (arrow).

(D) Middle ear mucosae were harvested and weighed on day 7 of each lineage from each episode (episode 1, n = 3; episodes 2–4, n = 6). The three independent mucosal (square) and effusion (triangle) lineages are indicated by the colors (red, blue, and green).

(E) Tissues were homogenized and the mucosal-associated bacterial burden was enumerated and normalized as colony forming units (CFUs) per milligram (mg) tissue. Color and symbols are consistent with (D).

(F) Effusions were collected by epitympanic tap of the middle ear bullae prior to dissection on day 7 of each episode. Bacteria were enumerated as CFU/mL of fluid. Colors and symbols are consistent with (D).

Statistical significance was determined using a two-tailed Student's t test with the mean and standard error of the mean (D) or geometric mean (E and F) indicated. Scale bars (B and C), 250 mm.
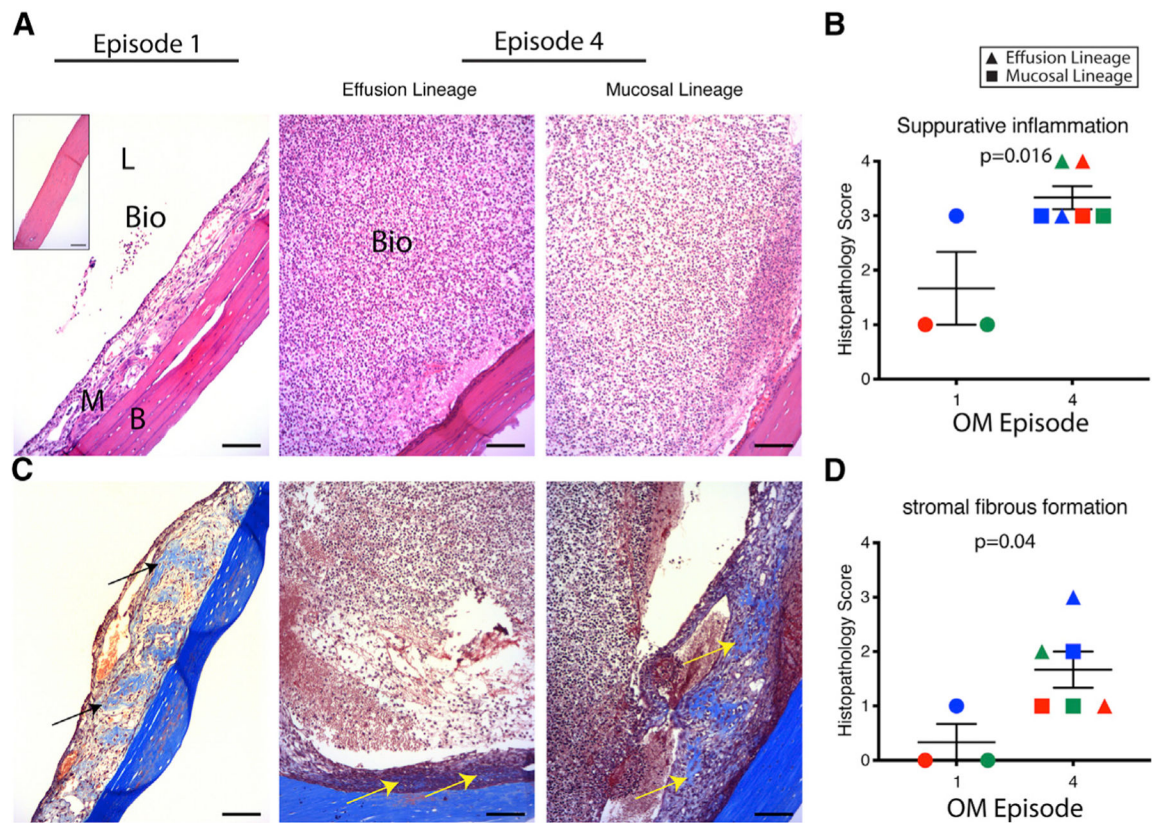
Figure 2. Suppurative Inflammation and Stromal Fibrosis Are Increased by the End of Episode 4

(A–D) On day 7 of episodes 1 and 4, middle ears were fixed, embedded, sectioned, deparaffinized, and stained with hematoxylin and eosin (H&E)n) (A and B) or and Masson's trichrome stain (C and D) for visualization by light microscopy. L, lumen; Bio, biofilm; M, mucosae; B, bone.

(A) Representative images of the middle ear mucosa, biofilm, and bony structures from episode 1 (n = 3) and the effusion and mucosal lineages of episode 4 (n = 6). Inset depicts the anatomy of a naive middle ear demonstrating that the naive mucosae is only 1 to 2 cells in thickness. In the images for episode 4, the biofilm fills the field of view and is composed of infiltrated immune cells and NTHI.

(B) Histopathologic scoring of the extent of suppurative inflammation between episodes 1 and 4. Color and symbols are consistent with Figure 1D. Pathologist was blinded to the experimental sample and statistical significance was determined by two-tailed Student's t test with the mean and standard error of the mean depicted.

(C) Masson's stain demonstrates the presence of stromal fibrosis (arrows) from representative samples from episodes 1 and 4 as described in (A). The images are all from different middle ear samples.

(D) Histopathologic scoring of the extent of stromal fibrosis between episodes 1 and 4. Color and symbols are consistent with Figure 1D. Pathologist was blinded to the experimental sample and statistical significance was determined by two-tailed Student's t test with the mean and standard error of the mean depicted. Scale bar, 100 μm.
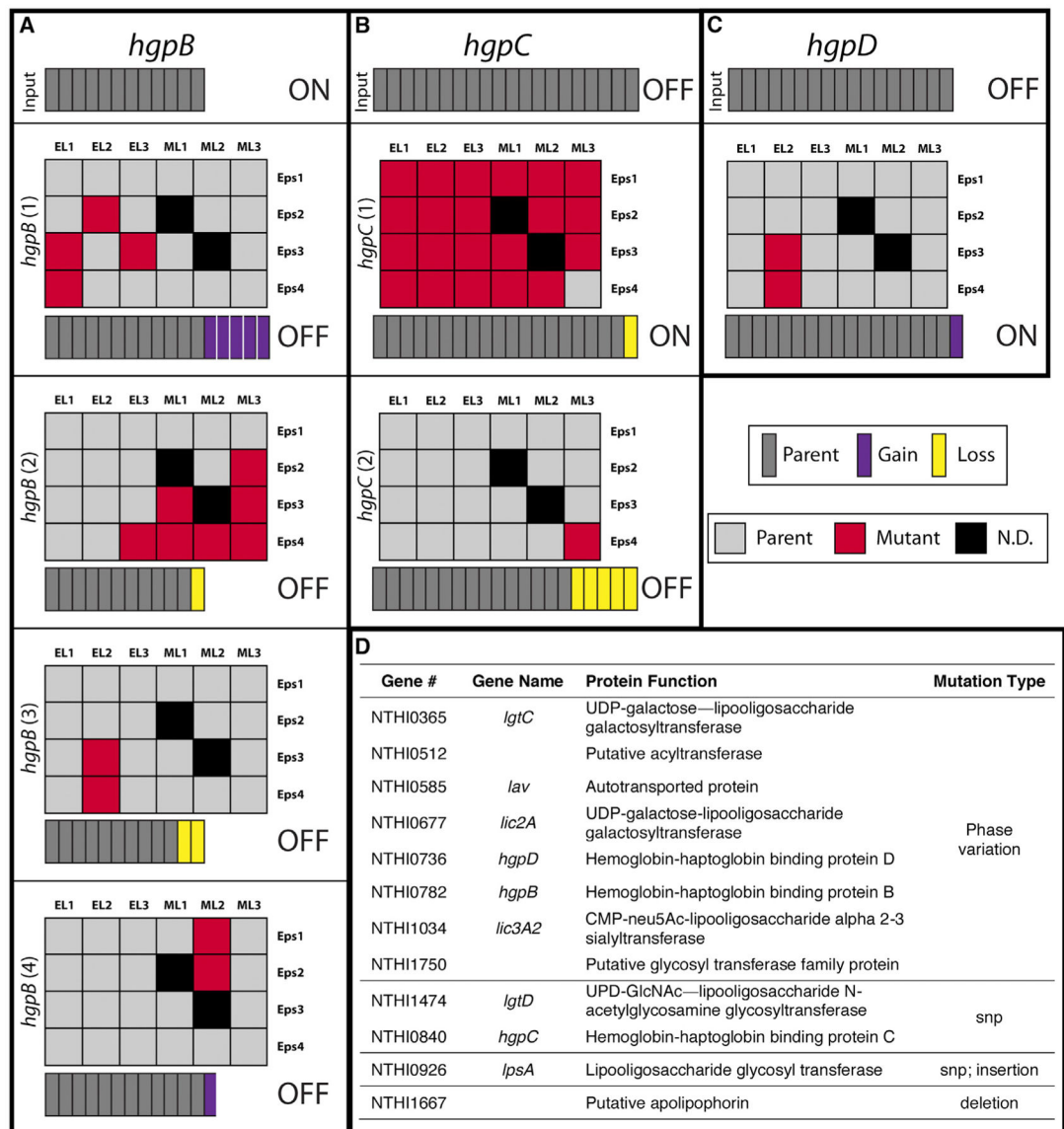
Figure 3. Phase Variation of Hemoglobin-Haptoglobin Binding Proteins (HgpB, HgpC, HgpD) during Sequential Episodes of OM

The number of tetranucleotide repeats (indicated as a gray rectangle) for the input strain was determined by Sanger sequencing performed in technical triplicate and is depicted at the top of each panel. The ON or OFF state of the parental input strain is indicated to the right of the number of repeats.

(A) The number of tetranucleotide repeats for each of the mutant forms detected for *hgpB* is indicated with a gain of repeats (purple) or loss of repeats (yellow). The effect of the mutation on the ON/OFF state is indicated to the right of the number of repeats. A matrix of the presence (red) or absence (gray) of each mutation (1–4) is presented for each episode (Eps 1–4) for each lineage (effusion lineage, EL 1–3; lineage, ML 1–3). The black squares indicate samples where NTHI could not be recovered from frozen mucosal samples and mutation status was not determined (ND).

(B) The number of tetranucleotide repeats, ON/OFF status, and presence or absence of mutations in *hgpC* are presented as described for (A).

(C) The number of tetranucleotide repeats, ON/OFF status and presence or absence of mutations in *hgpD* are presented as described for (A).

(D) The gene number, gene name, protein function, and mutation type for each of the 12 genes identified in this study.
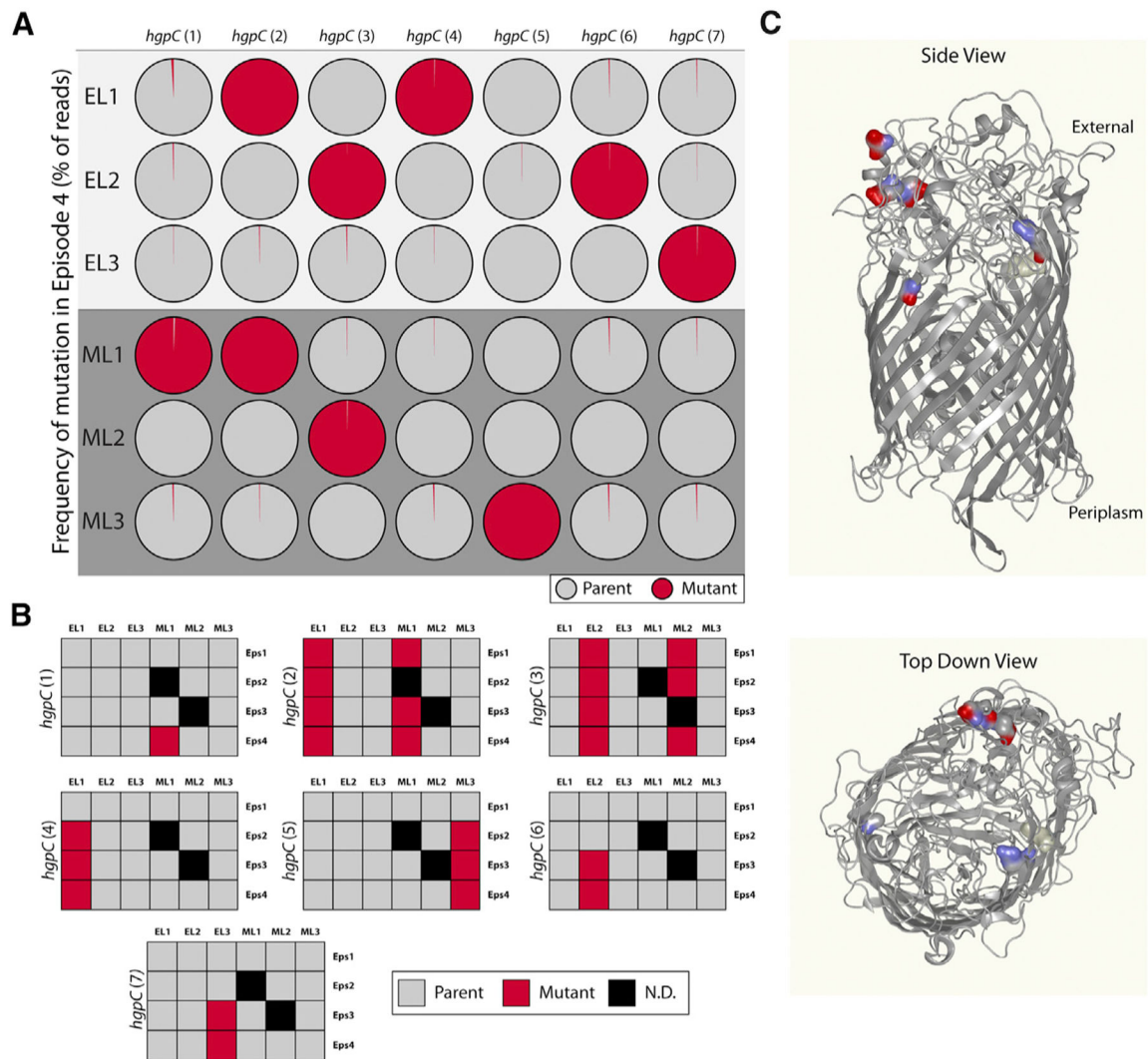
Figure 4. SNPs Are Observed in the Hemoglobin-Haptoglobin Binding Protein HgpC during Sequential Episodes of OM

(A) The frequency of mutations (*hgpC* 1–7) observed by whole genome sequencing at the end of episode 4 for each of the three effusion (EL 1–3) and mucosal (ML 1–3) lineages is depicted as a pie chart. The parental sequence is indicated in gray with the mutant sequence indicated in red. The specific gene modifications and outcomes are presented in Table S2.

(B) A matrix of the presence (red) or absence (gray) of each mutation, detected by Sanger sequencing (*hgpC* 1–7) performed in technical triplicate, is presented for each episode (Eps 1–4) for each lineage (EL 1–3; ML 1–3). The black squares indicate samples where NTHI could not be recovered from frozen mucosal samples and mutation status was ND.

(C) The HgpC-predicted 3-dimensional structure was determined in Phyre2 (Kelley et al., 2015). The position of the mutations is indicated with red or blue spheres, and the map to the external loops of the outer membrane barrel is presented in both the "side" and "top down" views.
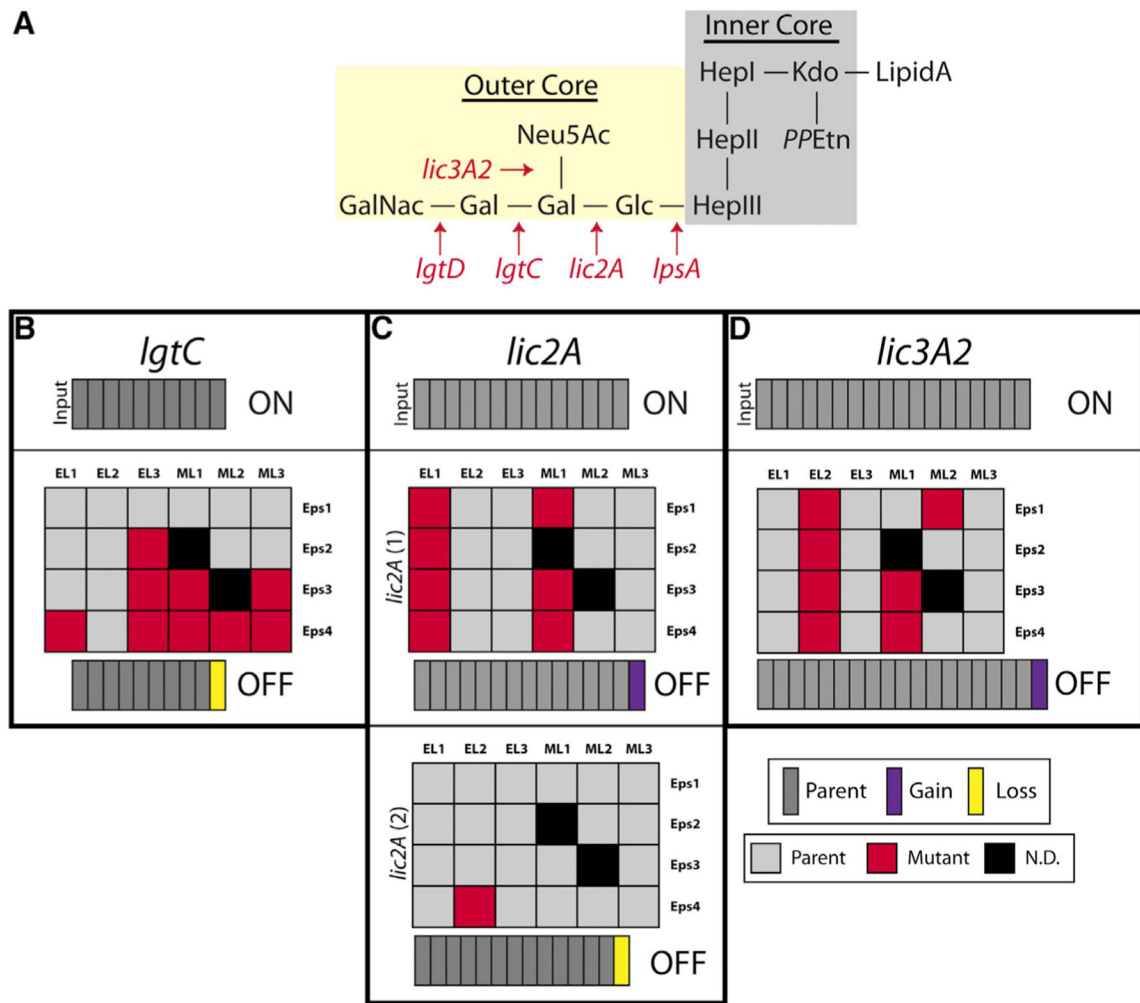
Figure 5. Phase Variation of LOS Modification Enzymes (LgtC, Lic2A, Lic3A2) during Sequential Episodes of OM

(A) Schematic representation of the predicted structure of LOS, based upon the *Haemophilus* strain Rd (Wong and Akerley, 2012). The predicted activity of each LOS enzyme that synthesizes the outer core is indicated in red.

(B–D) The number of tetranucleotide repeats (indicated as a gray rectangle) for the input strain was determined by Sanger sequencing performed in technical triplicate and is depicted at the top of each panel. The ON or OFF state of the parental input strain is indicated to the right of the number of repeats.

(B) The number of tetranucleotide repeats for the mutant detected for *lgtC* is indicated with the loss of one repeat (yellow). The effect of the mutation on the ON/OFF state is indicated to the right of the number of repeats. A matrix of the presence (red) or absence (gray) of the mutation is presented for each episode (Eps 1–4) for each lineage (EL 1–3; ML 1–3). The black squares indicate samples where NTHI could not be recovered from frozen mucosal samples and mutation status was ND.

(C) The number of tetranucleotide repeats for the two mutants detected for *lic2A* are indicated with the loss of one repeat (yellow) or gain of one repeat (purple). The ON/OFF

status and matrix demonstrating the presence or absence of two mutations in *lic2A* are presented as described for (B).

(D) The number of tetranucleotide repeats for the mutant detected for *lic3A2* is indicated with the gain of one repeat (purple). The ON/OFF status and matrix demonstrating the presence or absence of two mutations in *lic3A2* are presented as described for (B).
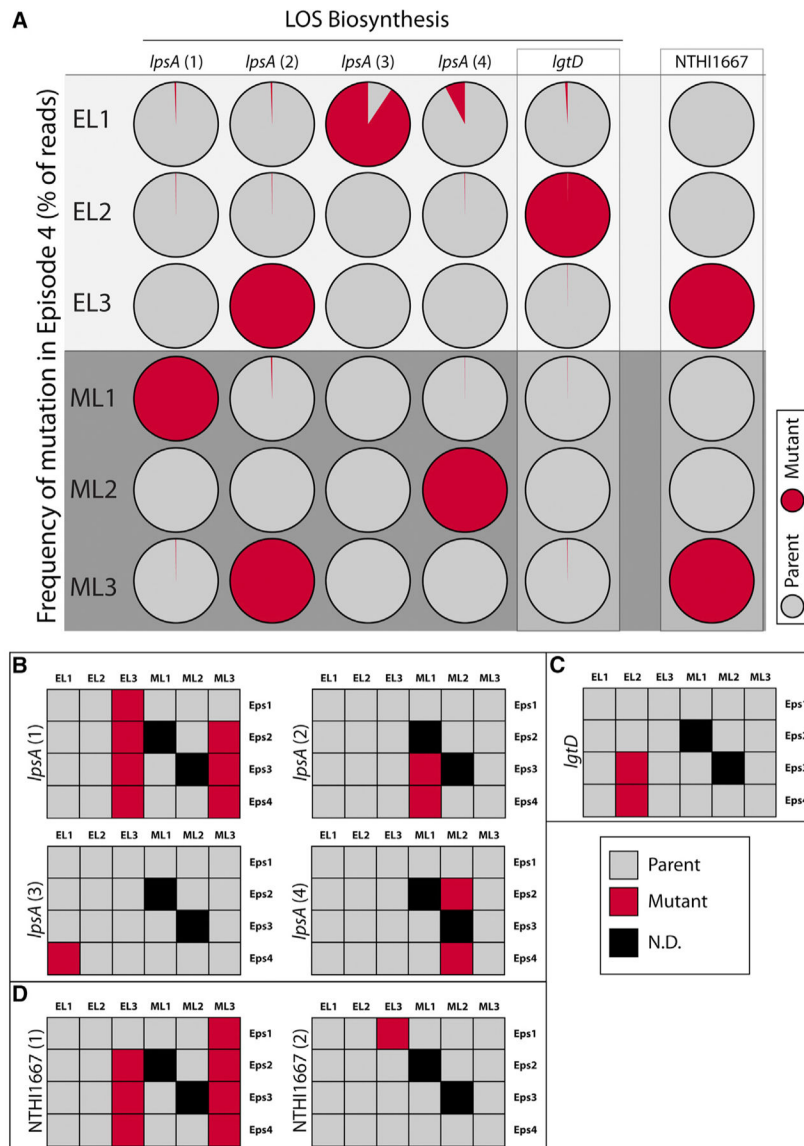
Figure 6. Non-phase Variable Genetic Mutations Are Observed in the LOS Biosynthetic Genes and One Hypothetical Gene during Sequential Episodes of OM

(A) The frequency of mutations (*lpsA* 1–4; *lgtD*; NTHI1667) observed by whole-genome sequencing at the end of episode 4 for each of the three effusion (EL 1–3) and mucosal (ML 1–3) lineages is depicted as a pie chart, as presented in Figure 4A. The specific gene modifications and outcomes are presented in Table S2.

(B) A matrix of the presence (red) or absence (gray) of each mutation, as detected by Sanger sequencing (*lpsA* 1–4) performed in technical triplicate, is presented for each episode (Eps 1–4) for each lineage (EL 1–3; ML 1–3).

(C) A matrix of the presence (red) or absence (gray) of the mutation in *lgtD* is presented for each episode (Eps 1–4) for each lineage (EL 1–3; ML 1–3).

(D) A matrix of the presence (red) or absence (gray) of each mutation (NTHI1667 1 and NTHI1667 2) is presented for each episode (Eps 1–4) for each lineage (EL 1–3; ML 1–3).
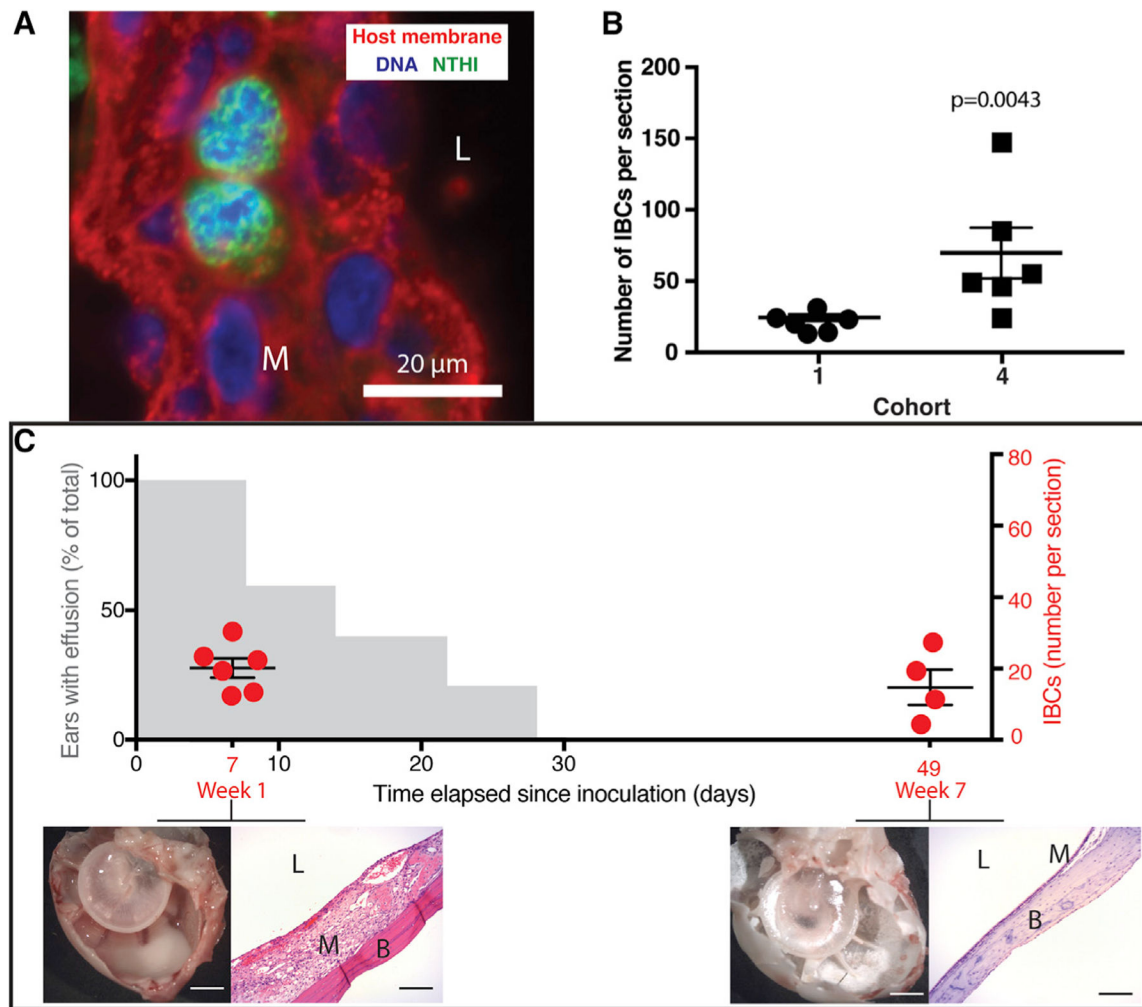
Figure 7. Sequential Episodes and Longevity of OM Promote IBC Formation

(A) Middle ears were processed for immunofluorescence microscopy using an antibody directed against NTHI outer membrane proteins and visualized with a secondary antibody conjugated to Alexa 488 to detect NTHI (green). Host cell membranes and DNA were visualized using wheat germ agglutinin (red) and Hoescht 33342 (blue), respectively. M, mucosae; L, lumen. Scale bar, 20 μm.

(B) The number of IBCs was quantified for each thin section for episodes 1 (n = 3) and 4 (n = 6) from both the effusion and mucosal lineages. Each data point represents the number of IBCs in a single thin section from all animals in the study. Statistical significance was determined using a two-tailed Student's t test; mean and standard error of the mean are depicted.

(C) The time to clearance (left y axis) of effusion from 10 ears over the natural course of infection, 28 days, is depicted in gray. The number of IBCs (right y axis) were enumerated from thin sections on day 7 (week 1, n = 3 independent ears) and 49 (week 7, n = 2 independent ears) of infection with the parental strain, and each red symbol represents the number from a single section. Error bars represent the mean and standard error of the mean. The gross images of representative middle ears used to quantify IBCs are depicted for days 7

and 49. The histological differences between the two time points are indicated by the H&E-stained sections. L, lumen; M, mucosae; B, bone. Black scale bar, 100 μm; white scale bar, 250 mm.

KEY RESOURCES TABLE

REAGENT or RESOURCE Antibodies	SOURCE	IDENTIFIER
Antibodies		
Anti-NTHI total outer membrane proteins	Raffel etal., 2013	N/A
Bacterial and Virus Strains		
NTHI strain 86–028NP	Harrison et al., 2005	N/A
Chemicals, Peptides, and Recombinant Proteins		
chocolate agar	Thermo Fisher Scientific	Cat# R01302
Brain Heart Infusion Medium	Thermo Fisher Scientific	Cat# B11059
β-nicotinamide adenine dinucleotide hydrate	Sigma-Aldrich	Cat# N7004
Bovine hemin	Sigma-Aldrich	H9039
Paraformaldehyde (16% solution, EM grade)	Electron Microscopy Services	15710
CAS-Block Histochemical Reagent	Thermo Fisher Scientific	008120
Alexa Fluor 488 conjugated Protein A	Thermo Fisher Scientific	P11047
Alexa Fluor 594 conjugated wheat germ agglutinin	Thermo Fisher Scientific	W11262
Hoechst 33342	Thermo Fisher Scientific	62249
ProLong Gold Antifade Mountant	Thermo Fisher Scientific	P36930
Image-iT FX Signal Enhancer	Thermo Fisher Scientific	I36933
Critical Commercial Assays		
Gentra Puregene Yeast/Bact. Kit	QIAGEN	158567
QIAquick PCR Purification Kit	QIAGEN	28106
Deposited Data		
Whole genome sequencing files	This study	Accession number for NIH Sequence Read Archive (SRA). SRA:PRJNA576916
Experimental Models: Organisms/Strains		
Chinchilla lanigera	Rauscher Chinchilla Ranch LLC, La Rue, OH	Outbred
Oligonucleotides		
Oligonucleotides	See Table S1	
Software and Algorithms		
Photoshop Creative Suite 3	Adobe	https://www.adobe.com
ImageJ	NIH	https://imagej.nih.gov/ij/
GraphPad Prism 7	GraphPad Software	https://www.graphpad.com/
Churchill	Kelly etal., 2015	http://churchill.nchri.org/
LaserGene15 suite	DNASTAR	https://www.dnastar.com
Other		
Axio Lab.A1 light microscope with an Axiocam ERc 5 s camera	Carl Zeiss, Inc.	N/A
Axiovert 200M inverted epifluorescence microscope with Apotome attachment	Carl Zeiss, Inc.	N/A
gentleMACS M homogenizer tubes	Miltenyi Biotec	130-093-236